NASA/CR—2018–219737

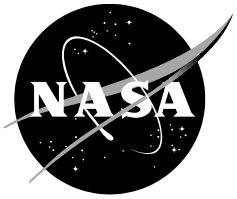

Generation of Performance Model for the Aeolian Wind Tunnel (AWT) Rotor at Reduced Pressure

Witold J. F. Koning
Science and Technology Corporation
Ames Research Center, Moffett Field, California

December 2018

NASA STI Program ... in Profile

Since its founding, NASA has been dedicated to the advancement of aeronautics and space science. The NASA scientific and technical information (STI) program plays a key part in helping NASA maintain this important role.

The NASA STI program operates under the auspices of the Agency Chief Information Officer. It collects, organizes, provides for archiving, and disseminates NASA's STI. The NASA STI program provides access to the NTRS Registered and its public interface, the NASA Technical Reports Server, thus providing one of the largest collections of aeronautical and space science STI in the world. Results are published in both non-NASA channels and by NASA in the NASA STI Report Series, which includes the following report types:

- TECHNICAL PUBLICATION. Reports of completed research or a major significant phase of research that present the results of NASA Programs and include extensive data or theoretical analysis. Includes compilations of significant scientific and technical data and information deemed to be of continuing reference value. NASA counterpart of peer-reviewed formal professional papers but has less stringent limitations on manuscript length and extent of graphic presentations.

- TECHNICAL MEMORANDUM. Scientific and technical findings that are preliminary or of specialized interest, e.g., quick release reports, working papers, and bibliographies that contain minimal annotation. Does not contain extensive analysis.

- CONTRACTOR REPORT. Scientific and technical findings by NASA-sponsored contractors and grantees.

- CONFERENCE PUBLICATION. Collected papers from scientific and technical conferences, symposia, seminars, or other meetings sponsored or co-sponsored by NASA.

- SPECIAL PUBLICATION. Scientific, technical, or historical information from NASA programs, projects, and missions, often concerned with subjects having substantial public interest.

- TECHNICAL TRANSLATION. English-language translations of foreign scientific and technical material pertinent to NASA's mission.

Specialized services also include organizing and publishing research results, distributing specialized research announcements and feeds, providing information desk and personal search support, and enabling data exchange services.

For more information about the NASA STI program, see the following:

- Access the NASA STI program home page at http://www.sti.nasa.gov

- E-mail your question to help@sti.nasa.gov

- Phone the NASA STI Information Desk at 757-864-9658

- Write to:
  NASA STI Information Desk
  Mail Stop 148
  NASA Langley Research Center
  Hampton, VA 23681-2199

NASA/CR—2018–219737

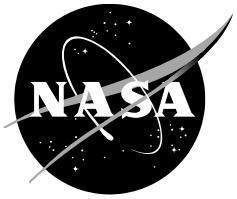

Generation of Performance Model for the Aeolian Wind Tunnel (AWT) Rotor at Reduced Pressure

Witold J. F. Koning
Science and Technology Corporation
Ames Research Center, Moffett Field, California

National Aeronautics and
Space Administration

Ames Research Center
Moffett Field, CA 94035-1000

December 2018

Acknowledgments

The author would like to thank Eduardo Solis for 3D-scanning and processing the AWT rotor, Alan Wadcock for many helpful discussions, and Bill Warmbrodt for his unwavering support.

Special thanks to Geoffrey Ament for his assistance in AWT rotor specifics and his inspiring work ethic. Numerous interns and researchers at the Aeromechanics Branch have contributed to the current status of this research—without them the current understanding would not have been achieved. A special thank you to Natalia Perez and Marcus Johansson for their large contributions to this project.

Table of Contents

List of Figures

List of Tables

Nomenclature

Abbreviations

ADM	Actuator-Disk Model
AWT	Aeolian Wind Tunnel (rotor)
BEM	Blade-Element Model
C81Gen	C81 Generator
CAD	Computer Aided Design
CFD	Computational Fluid Dynamics
CPU	Central Processing Unit
DNS	Direct Numerical Simulation
GPU	Graphics Processing Unit
GRS	Grid Resolution Study
JPL	Jet Propulsion Laboratory
LSB	Laminar Separation Bubble
MARSWIT	Mars Wind Tunnel
MH	Mars Helicopter
PAL	(NASA Ames) Planetary Aeolian Laboratory
RANS	Reynolds-Averaged Navier-Stokes
RotCFD	Rotorcraft CFD
RotUNS	Rotorcraft Unstructured Solver
SA	Spalart-Allmaras (turbulence model)
UAV	Unmanned Aerial Vehicle
VTOL	Vertical Takeoff and Landing

Symbols

c	airfoil chord
c_d	section drag coefficient
c_l	section lift coefficient
f	airfoil camber
M	Mach number
p	pressure
r	radial coordinate
R	blade radius; gas constant
Re	Reynolds number
t	airfoil thickness
T	temperature
x, y	local coordinates
y^+	nondimensional wall distance

Greek

γ	specific heat ratio
θ	blade twist
μ	dynamic viscosity
ρ	density

Subscripts

c	chord based
max	maximum

Generation of Performance Model for the Aeolian Wind Tunnel (AWT) Rotor at Reduced Pressure

Witold J. F. Koning[1]

Ames Research Center

Summary

The NASA Jet Propulsion Laboratory (JPL) designed the Mars Helicopter (MH) in collaboration with AeroVironment Inc., NASA Ames Research Center, and NASA Langley Research Center to explore the possibility of a vertical takeoff and landing (VTOL) Unmanned Aerial Vehicle (UAV) for flight on Mars [1]. A 40-inch-diameter Aeolian Wind Tunnel (AWT) rotor, roughly approximating the proposed MH design by JPL, was tested in forward flight at Mars atmospheric pressure at the NASA Ames Planetary Aeolian Laboratory (PAL) in support of MH research efforts. This report describes the generation of the rotor model used to correlate with that experimental effort as reported by Ament and Koning [2].

The 40-inch-diameter rotor was 3D-scanned and transformed into an airfoil deck. The scanned rotor airfoil sections are analyzed using C81 Generator (C81Gen) to generate the sectional aerodynamic coefficients for comprehensive analyses. A mid-fidelity computational fluid dynamics (CFD) simulation using Rotorcraft CFD (RotCFD) is pursued to efficiently estimate rotor hover and forward flight performance. Simulations at two pressures, 7 mbar (approximate Martian atmospheric pressure) and 1018 mbar (1 atmosphere), are performed to gain an understanding of the performance differences and Reynolds number effects observed.

Experimental 1-atmosphere thrust for single- and dual-rotor isolated hover cases correlate well with the modeled rotor. Performance results at reduced pressure (7 mbar) show a drastic decrease in lift for equivalent RPMs tested at 1 atmosphere. Although this is primarily due to pressure reduction, Reynolds number effects also contribute to this decrease, as airfoil lift and drag coefficients are affected when compared with 1-atmosphere results. Further, simulated rotor power coefficient shows drastic increases at reduced pressures, attributed to laminar boundary layer separation, as described in Koning et al. [3] for the MH rotor analysis.

PAL experimental Martian Surface Wind Tunnel (MARSWIT) results are presented in the paper by Ament and Koning [2]. The very low Reynolds number range is currently not well understood and presents various challenges for both experimentation and simulation.

[1] Science and Technology Corporation, NASA Research Park, Moffett Field, CA 94035.

Introduction

The NASA Jet Propulsion Laboratory (JPL) designed the Mars Helicopter (MH) in collaboration with AeroVironment Inc., NASA Ames Research Center, and NASA Langley Research Center to explore the possibility of a vertical takeoff and landing (VTOL) Unmanned Aerial Vehicle (UAV) for flight on Mars [1]. The design of the UAV is a solar powered coaxial helicopter with a mass of roughly 1.8 kg and a 1.2-m rotor diameter. The design serves as a technology demonstrator, eventually intended for low-altitude flight on Mars. Koning et al. [3] contains a report on the rotor, low Reynolds number effects, and rotor aerodynamic performance.

In an effort to further understand rotor behavior under exotic flight conditions, experimental testing was performed at NASA Ames Research Center. A 40-inch-diameter twisted 40x22 rotor (AWT rotor), roughly approximating the proposed MH design by JPL, was tested in forward flight at Mars atmospheric pressure at the NASA Ames Planetary Aeolian Laboratory (PAL). The goal of this experiment was to collect rotor thrust, rotational speed, power, torque, and acoustics measurements [2] using both single and dual (co-rotating) configurations. Ament et al. [4] contains the full experimental data report. The rotor had previously been used for hover testing in JPL's 25-foot Space Simulator.

This report describes the generation of the rotor model and subsequent analyses used to correlate with experimental efforts as referenced in Ament and Koning [2]. The 40-inch-diameter rotor was 3D-scanned and transformed into an airfoil deck for use in comprehensive analyses. A mid-fidelity computational fluid dynamics (CFD) simulation using Rotorcraft CFD (RotCFD) is pursued to efficiently estimate rotor hover and forward flight performance values. Simulations at two pressures, 8 mbar and 1018 mbar (1 atmosphere), are performed to gain an understanding of the performance differences and Reynolds number effects observed. Hover tests at 1 atmosphere, as well as Martian Surface Wind Tunnel (MARSWIT) forward flight results, are discussed in Ament and Koning [2].

Aeolian Wind Tunnel (AWT) Rotor Preprocessing

NASA Ames Research Center has been researching the feasibility of vertical lift aerial vehicles on other planets such as Mars. The atmospheric conditions of Mars provide a unique combination of low Reynolds number flow and compressible flow aerodynamics [5]. Early isolated rotor hover testing at reduced pressure was done by Young et al. [6]; the experiments were performed at the NASA Ames PAL, which can be reduced to the atmospheric pressure of Mars. Although an initial attempt was made to predict rotor hover performance by Corfeld et al. [7], significant disagreements exist between the experimental data and CFD predictions.

The AWT rotor is 40 inches in diameter, approximately 83 percent scale of the proposed MH rotor diameter. The rotor was initially chosen for 1-atmosphere hover testing in JPL's 25-foot Space Simulator. For this reason, it was selected for investigative forward flight testing at NASA Ames.

3D Scan of Rotor

To generate the AWT rotor C81 airfoil tables, the propeller blade was measured using a Creaform MetraScan 70, a 3D optical laser scanner. The resulting point cloud is processed by fitting profile curves and surfaces to reconstruct the 3D CAD model (Figure 1).

The laser was selected for its ability to measure millions of discrete surface points with high accuracy (0.0025 in. or 0.064 mm) in a short period of time. The fitted curves and surface patches are then imported into Rhinoceros 3D (Rhino) to extract and generate 2D airfoil cross-section curves. The 2D cross-section curves are then divided by 500 equally spaced points in 23 sections, as shown in Figure 2.

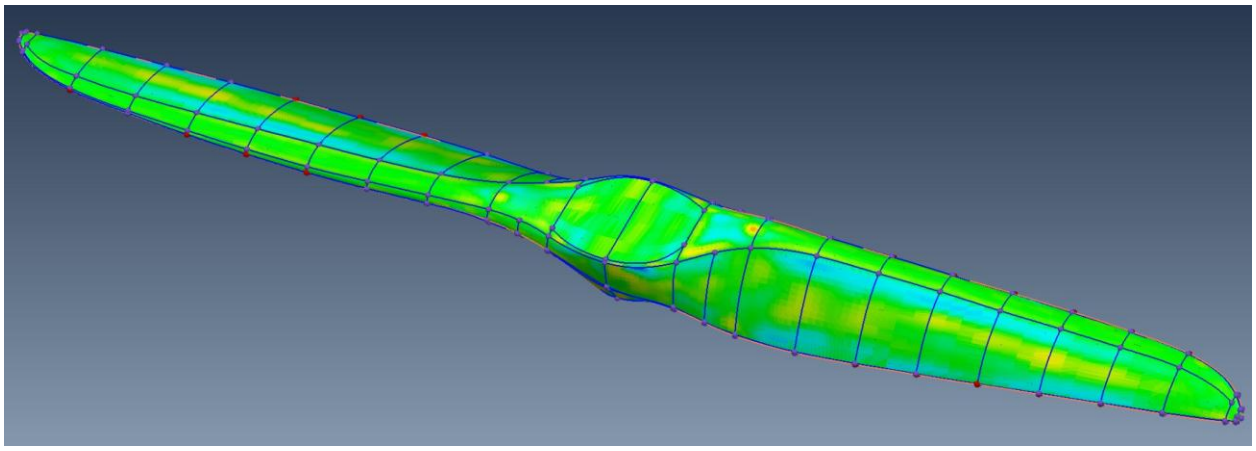

Figure 1. Fitting analyses are performed to verify curve and surface accuracy.

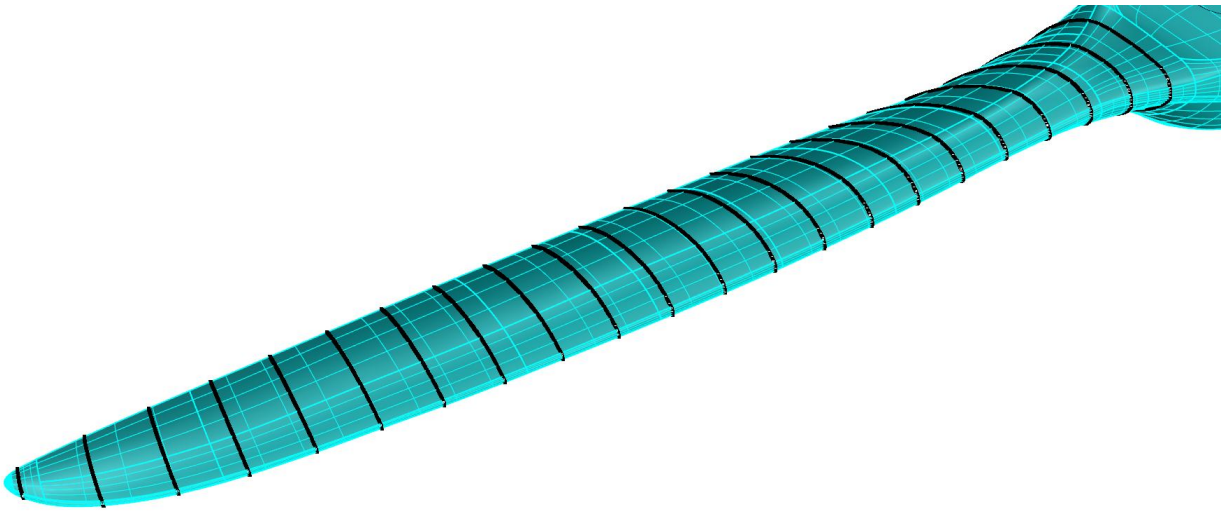

Figure 2. The propeller blade is divided into 23 sections for 2D airfoil profile extraction.

The 2D airfoil profiles are processed to normalize the airfoil coordinates, and to obtain chord and twist distributions for each radial station. The airfoils are used to extract the magnitude and location of maximum thickness and camber for the airfoil at each radial station.

Critical CFD Station Selection

The thickness and camber of each section, as well as the location of maximum thickness and camber, are extracted from the profiles as shown in Figure 3. In turn, these are used to determine the critical radial stations that will be analyzed using CFD. Other features that are not captured by these parameters (e.g., leading edge radius, trailing edge shape, etc.) are observed visually by plotting airfoil profiles to ensure that no large changes in airfoil characteristics are neglected.

The radial stations at r/R = 0.29, 0.58, and 0.78 were chosen as the critical airfoils, shown in Figure 4. The rotor model in RotCFD linearly interpolates C81 data; it is good practice therefore to verify that the chosen stations are at local minima, local maxima, or discontinuities along the curve (Figure 3). The chosen radial stations effectively produce a bilinear thickness and camber distribution in RotCFD. Care must be taken to properly model the region outside of the chosen radial stations (outmost root and tip regions). The panel density of the profiles is improved using XFOIL [8], which maintains the density along the panel and provides a satisfactory density ratio near steeper gradients (e.g., leading and trailing edges).

The airfoils at r/R = 0.17 and r/R = 0.99 were discarded because of the dissatisfactory shape obtained after scanning.

The differences between the chosen airfoils are clear, especially airfoil crests moving downstream for increased radial station. Table 1 shows the thickness and camber properties of selected critical stations.

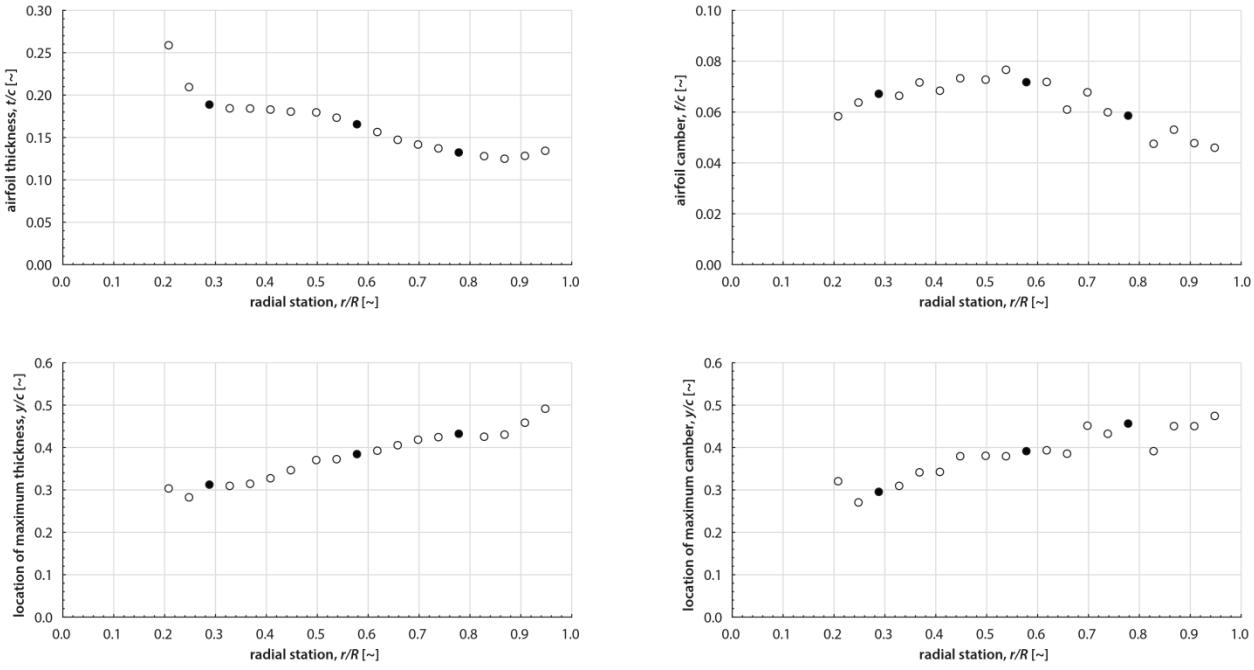

Figure 3. AWT rotor airfoil thickness and camber distribution (open symbols: radial stations; closed symbols: critical stations).

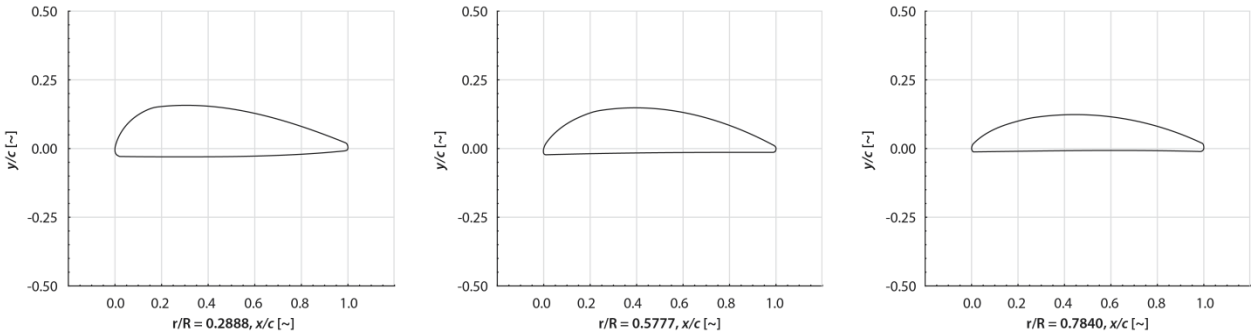

Figure 4. AWT rotor critical stations.

Table 1. AWT critical radial station selection.

#	r/R (~)	t/c (~)	$x_{(t/c)max}$	f/c	$x_{(f/c)max}$	Name
4	0.289	0.188	0.310	0.067	0.293	station 1
11	0.578	0.164	0.382	0.071	0.389	station 2
16	0.784	0.131	0.430	0.058	0.454	station 3

Upon airfoil normalization, a script extracts the pitch angle and chord length. RotCFD uses the chord and twist values to create the appropriate rotor model source terms from the airfoil coefficients in the C81 deck. Figure 5 shows the obtained chord and twist distributions from the scanned blade. The script faced challenges identifying "ambiguous" leading or trailing edges along the blade, resulting in scatter observed in Figure 5. Since the rotor has no observable discontinuities in twist or chord, the outliers are identified and discarded. Twist distribution is more troublesome but is corrected after the outliers are removed.

Discarded values for the chord and twist distribution are grayed-out in Figure 5.

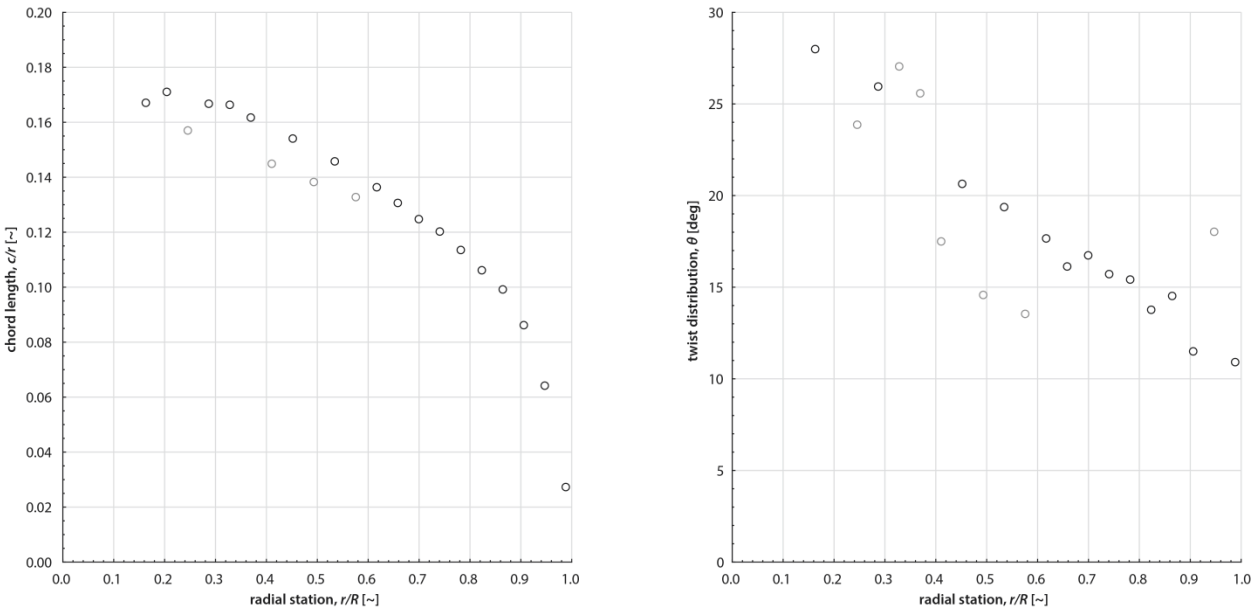

Figure 5. Estimation of AWT rotor chord and twist distribution.

Reynolds Number Effects at Reduced Pressure

Reduced atmospheric density near the Martian surface, combined with the MH's relatively small rotor, results in extremely low chord-based Reynolds number flows. Furthermore, the low density and low Reynolds number reduce the lifting force and lifting efficiency, respectively, which is only partially compensated by a lower gravitational acceleration of around $g = 3.71$ m/s^2 compared to Earth's gravitational acceleration ($g = 9.81$ m/s^2). Table 2 gives an overview of the operating conditions of interest on Mars and the lowest pressure that the PAL facility can reach. The static pressure is obtained through the equation of state.

A more in-depth overview of the Martian atmosphere, its composition, and implications of the low atmospheric pressure and density are shown in Koning et al. [3]. The AWT rotor chord-based Reynolds numbers are roughly $Re_c < 10^5$ when tested at the lowest pressure in the PAL, approximately 7 mbar. This range of Reynolds numbers are used synonymously with "low Reynolds numbers" from here on. The significance of the low Reynolds number is the prevailing of viscous forces on the airfoils over the inertial forces of the flow. However, this scale of Reynolds numbers is currently not well understood [9].

At low Reynolds numbers, the drag coefficient increases approximately an order of magnitude. The lift coefficient remains an order of 1 but is also reduced for lower Reynolds numbers [10], [14], [15]. This greatly reduces the obtainable lift-to-drag ratio at very low Reynolds numbers. The rotor model in this report is only generated for use at around 7 mbar and 1018 mbar, since intermediate pressures can be subject to boundary layer transition (and laminar separation bubbles (LSBs)), which are difficult to properly predict and simulate. Figure 6 and Figure 7 show the influence of the Reynolds number on aerodynamic coefficients.

These figures reinforce the argument that rotor model generation, especially around the critical Reynolds number transition region (shaded region of Figure 7), must receive extra consideration. Schmitz [16] describes the influence and implication of these low Reynolds numbers, and indicates that proper experimental values are very difficult to obtain as accidental tripping of the boundary layer significantly affects aerodynamic coefficients (in particular, the drag coefficient). Currently, the only way to correctly model the flow physics at the transitional low Reynolds numbers is to use Direct Numerical Simulation (DNS). Unfortunately, the cost of DNS simulations is prohibitive for the large number of simulations required to generate an airfoil database [3]. Some transition models are developed that allow RANS methods to predict transition in LSBs with increasing success.

Table 2. Operating conditions for Mars condition 1-3.

Variable	Earth SLS	Mars Min	Mars Max	AWT Min
Density, ρ (kg/m^3)	1.225	$1.500 \cdot 10^{-2}$	$2.000 \cdot 10^{-2}$	$8.000 \cdot 10^{-3}$
Temperature, T (K)	$2.882 \cdot 10^2$	$2.482 \cdot 10^2$	$1.932 \cdot 10^2$	$2.882 \cdot 10^2$
Gas Constant, R (m^2/s^2/K)	$2.871 \cdot 10^2$	$1.889 \cdot 10^2$	$1.889 \cdot 10^2$	$2.870 \cdot 10^2$
Specific Heat Ratio, γ (~)	1.400	1.289	1.289	1.400
Dynamic Viscosity, μ (Ns/m^2)	$1.750 \cdot 10^{-5}$	$1.130 \cdot 10^{-5}$	$1.130 \cdot 10^{-5}$	$1.750 \cdot 10^{-5}$
Static Pressure, p (Pa)	$1.013 \cdot 10^5$	$7.031 \cdot 10^2$	$7.297 \cdot 10^2$	$6.617 \cdot 10^2$

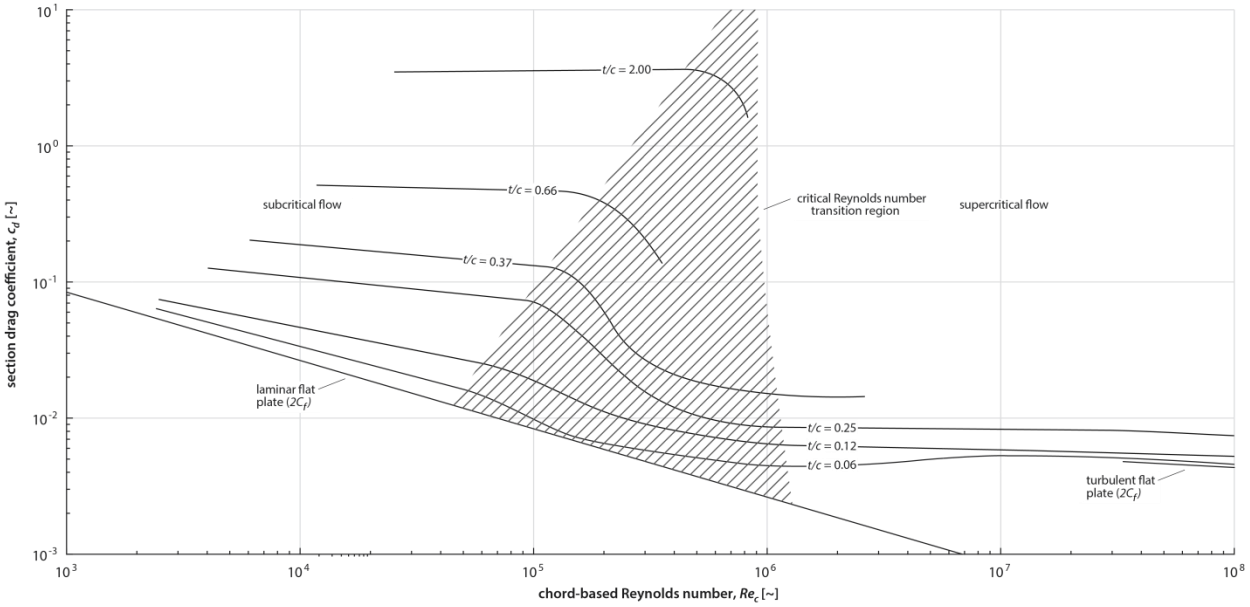

Figure 6. Reynolds number versus section drag coefficient ($c_l \approx 0$; created referring to ref. [10]).

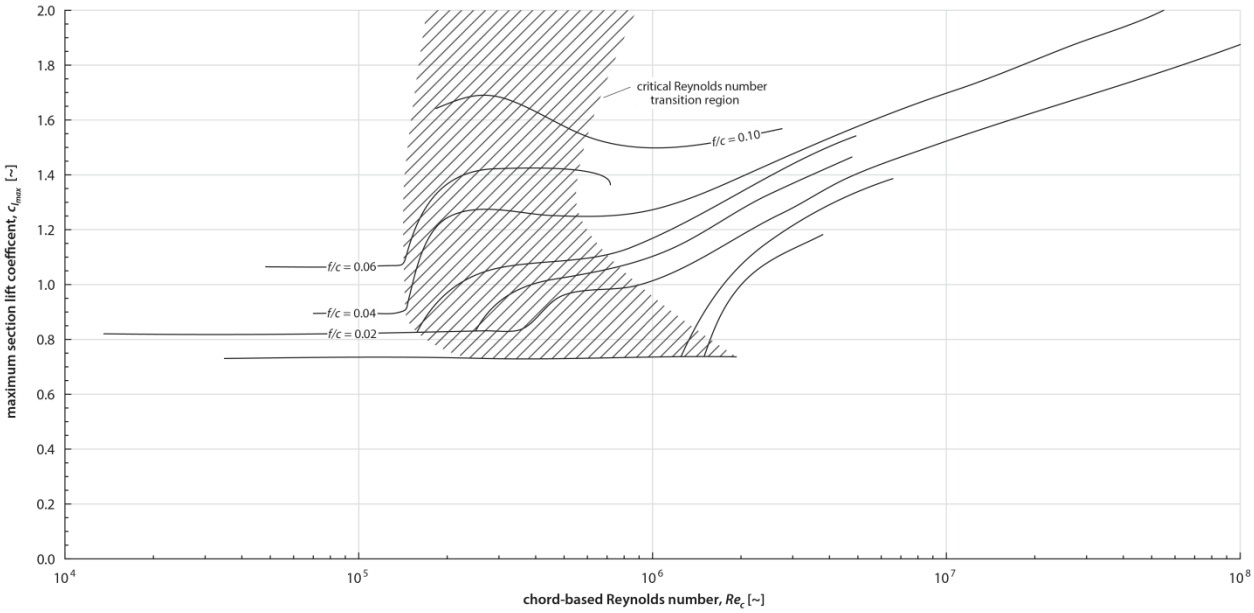

Figure 7. Section lift versus Reynolds number (t/c = 0.08 – 0.10; created referring to ref. [15]).

The paper by Koning et al. [3] describes the implications of the largely subcritical Reynolds number range experienced in the Martian atmospheric pressure and density range. Good correlation was found for the Figure of Merit of the MH rotor compared to experimental tests at low densities.

For the rotor model at Earth's atmosphere, the rotor is approximated to have "fully turbulent" flow for the 2D CFD analysis; this is due to the relatively high Reynolds number distribution over the blade span.

C81 Generator (C81Gen)

A Reynolds-Averaged Navier-Stokes (RANS)-based approach using C81Gen is used to generate the aerodynamics coefficients for the airfoil deck, similar to that performed in Koning et al. [3]. C81Gen is developed to create C81 format tables for a user-specified range of alpha-Mach pairs. C81Gen runs the 2D time-dependent compressible RANS solver ARC2D with structured body-fitted viscous gridding. The program uses an implicit finite-difference method to solve 2D thin-layer Navier-Stokes equations. C81Gen runs an alpha-Mach pair on each central processing unit (CPU) core (or thread) available on a machine in parallel.

Within C81Gen, the flow type can be set to "fully turbulent," fully laminar, or set to use pre-specified transition locations. C81Gen uses the Spalart-Allmaras (SA) turbulence model [3]. The SA turbulence model activates after $Re_c = 20{,}000$ to $60{,}000$, based on Mach number [17] and should not be used as a (turbulence) transition model. The turbulence model was indeed found not to alter the results in the linear range of the coefficients for the 7-mbar simulations, but it seemed to have a slight effect for the very high, stalled, angles of attack. For the rotor model at Earth's atmosphere, the rotor is approximated to have "fully turbulent" flow for the 2D CFD analysis; i.e., the turbulence production terms are active. A transition model would be preferable.

The time grid was chosen to be accelerated non-time-accurate with automatic switching to time-accurate if needed, based on residual values. In the case of a time-accurate simulation, the coefficients will be based on the average periodic behavior. For this study C-grids were used, and all airfoils have a normalized chord length of $c = 1.00$ with the far field located at $50c$. For the C-grid, the number of points in streamwise, normal, and wake direction are specified. The y^+ value was kept around $y^+ \approx 1.00$ for all cases investigated.

Parameters for Critical Airfoil Stations

Table 3 shows the suggested alpha-Mach pairs to be analyzed in C81Gen. The angle-of-attack range is chosen to be substantial because of the absence of collective/cyclic control on the "fixed" AWT rotor and the relatively high twist observed over the blade. The Mach numbers are modest and chosen to incorporate hover with some range to allow for moderate advance ratios.

The C81 files obtained will be stitched with experimental (1-atmosphere) data for a NACA 0012 airfoil to encompass the entire range of angles of attack possible.

Table 3. AWT C81 alpha-Mach pair input parameters.

		Angle of Attack, a (deg)			Mach Number, M (~)		
Station	Airfoil	Start	Interval	End	Start	Interval	End
1	Station 1	-10	1.0	30	0.10	0.10	0.30
2	Station 2	-10	1.0	30	0.10	0.10	0.40
3	Station 3	-10	1.0	30	0.10	0.10	0.50

Grid Resolution Study (GRS)

The absence of experimental results limited the GRS to the drag-count resolution. It was deemed further resolution—and therefore run time—was not necessary until test results are available. Figure 8 shows the global structured viscous C-grid and a close-up of the gridding in the near field airfoil profile.

One-atmosphere (1018-mbar) GRS results are shown in Figure 9. The grid settings for each grid number are presented in Table 4.

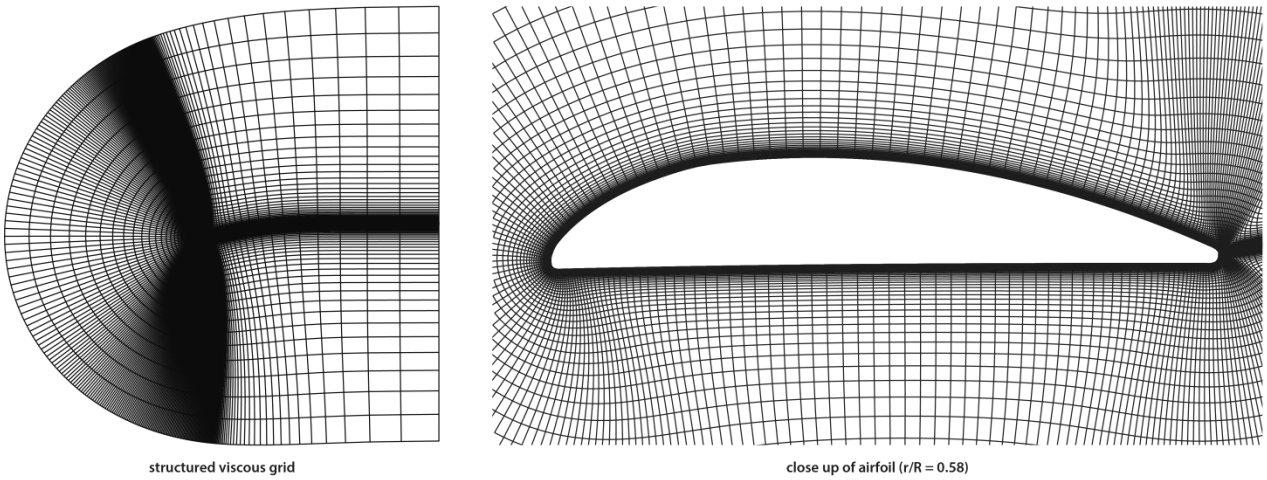

Figure 8. C81Gen structured grid around airfoil at r/R = 0.58.

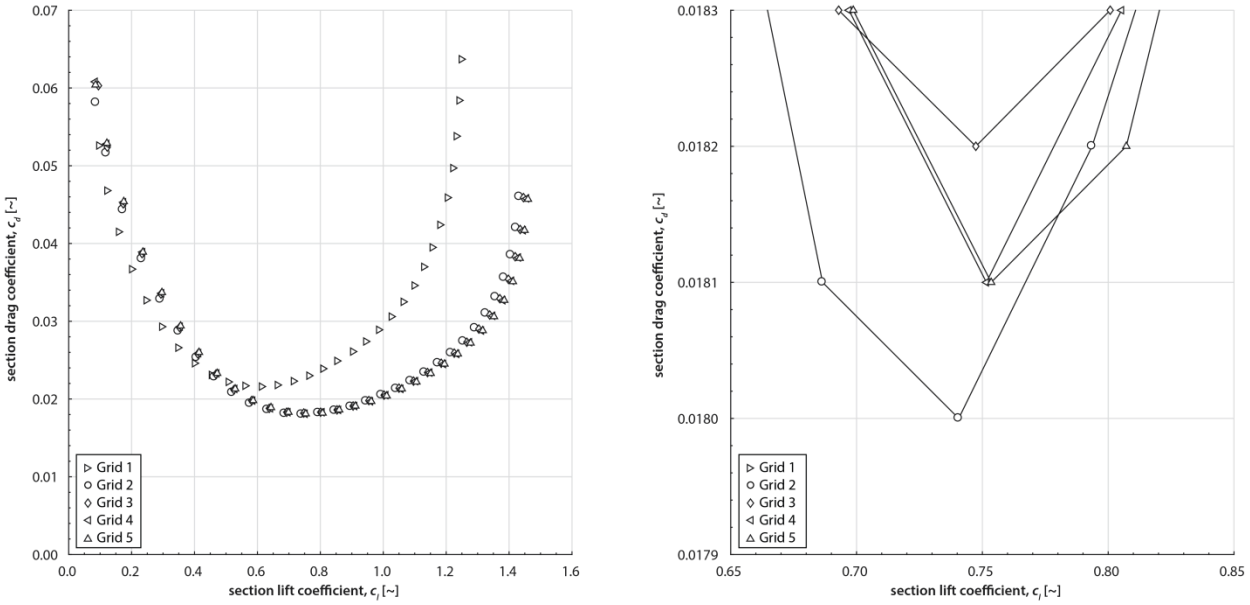

Figure 9. GRS at Earth's atmosphere (M = 0.5, y^+ = 1.0, and r/R = 0.78).

Table 4. Grid settings for the GRS.

Grid	Streamwise Points	Normal Points	Wake Points	y^+ ($M = 1.0$)
1	101	33	17	1.00
2	301	101	51	1.00
3	501	167	83	1.00
4	701	233	117	1.00
5	901	301	151	1.00

All but the first grid study produce $c_{d,\min}$ estimates within 1 to 2 drag counts (c_d = 0.0001 to 0.0002) from each other. For y^+ = 0.5 similar results with same minimum drag estimates are obtained. Results for the 7-mbar GRS are presented in Figure 10.

The increase in drag coefficient between the two pressures is substantial but expected. At low c_l values (or angle of attack), irregular behavior is attributed to reverse stall of the airfoils. C81Gen uses the thin layer RANS equations, producing results quickly, compared to the "full" RANS equations, at the cost of reduced simulation fidelity.

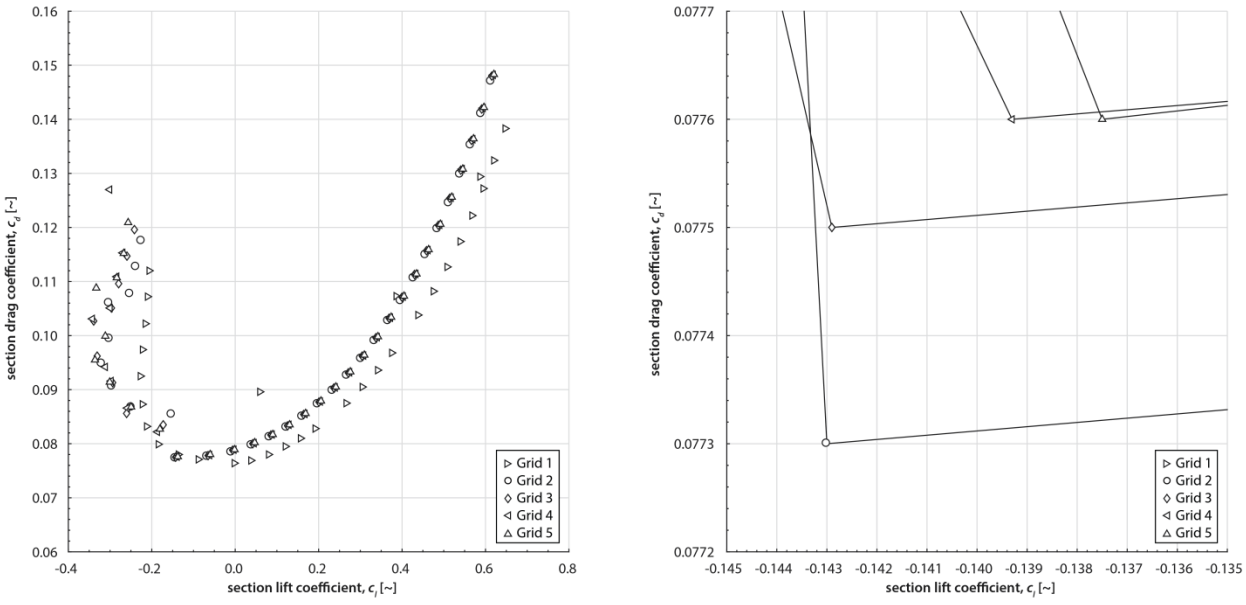

Figure 10. GRS at 7 mbar (M = 0.5, y^+ = 1.0, and r/R = 0.78).

C81 Airfoil Deck

Because the (fixed) rotor does not allow for collective (or cyclic) changes, the angles of attack over the blade span are expected to be higher than for "regular" helicopter blades. The angles of attack must be monitored in the simulation to not exceed the simulated range of angles of attack under various flight conditions, to ensure proper performance estimates. Figure 5 shows the substantial twist distribution that will produce relatively high angles of attack compared to a "regular" helicopter rotor.

Rotorcraft Computational Fluid Dynamics (RotCFD)

The mid-fidelity CFD software RotCFD [18] is used to perform an analysis of the rotor performance. RotCFD models the rotor through a blade-element model (BEM) or actuator-disk model (ADM), which uses an airfoil deck (C81 files generated by C81Gen) as input. The rotor is then modeled in a CFD (RANS) flow field through the momentum it imparts on the flow with a realizable k-ε turbulence model with special wall function. This method allows for good rotor performance estimates, while also simulating interactions with wind tunnels or airframes [19], [20]. RotUNS is a submodule of RotCFD, using an unstructured grid with the possibility of simulating multiple rotors and bodies in the flow field. RotUNS is used for all simulations unless otherwise noted. Both single- and dual-rotor configurations were modeled in RotUNS, in line with the projected experiments [2]. Figure 11 shows the RotCFD GUI and the control volume for the isolated hover cases.

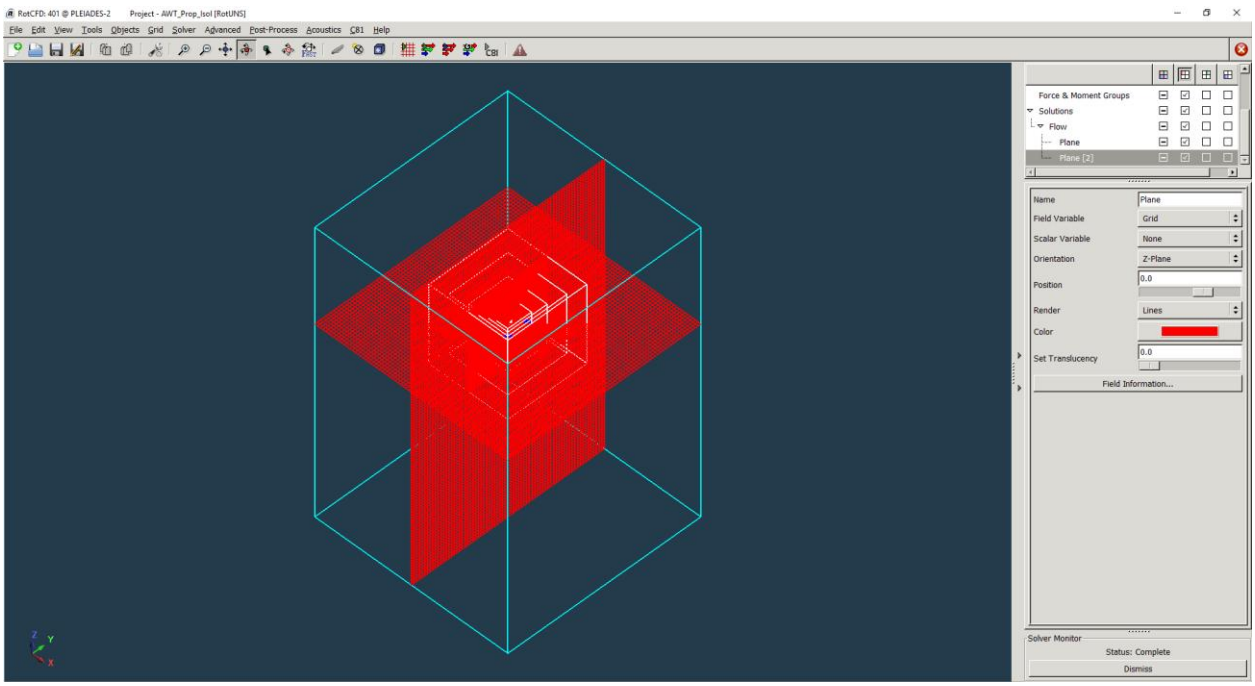

Figure 11. RotCFD (RotUNS) screenshot showing grid planes for isolated hover case.

Case Setup for Isolated Hover

The flow field for a rotor in hover was set up as a control volume with roughly 2.5 diameters above and 5 diameters below the rotor disk. The rotor tip path was cleared by around 2.5 diameters in the tip path plane. In the rotor near-field (within roughly a diameter of the rotor disk), the grid density is progressively increased to resolve the near-rotor flow more accurately. All boundary conditions are pressure-type, except for the bottom plane that is modeled as a mass-outflow correction to allow the wake to "exit" the control volume.

The general grid sizing is obtained from Koning et al. [19]. Afterwards the grid density is, however, vastly increased (around 10-fold) because of RotCFD advancements in computational efficiency. The increased efficiency is mostly due to the program's capability to run in parallel on graphics processing units (GPUs) [21] (computations are performed using OpenCL versus the previously used OpenMP framework). Figure 12 shows the side and top view of the grid, with the white line indicating the rotor disk. The grid was chosen to have a cell count of around 6 million; this refinement was chosen to achieve a balance in flow refinement and simulation time.

Case Setup for Forward Flight in MARSWIT

The grid for the tunnel is based on the isolated hover grid but constrained to the tunnel test section dimensions for ease of calculation. The walls and floors are modeled as viscous walls, the inlet is set to a predefined inlet velocity, and the tunnel outlet is modeled as a mass-outflow condition. Figure 13 shows the unstructured grid, with the white line indicating the rotor disk.

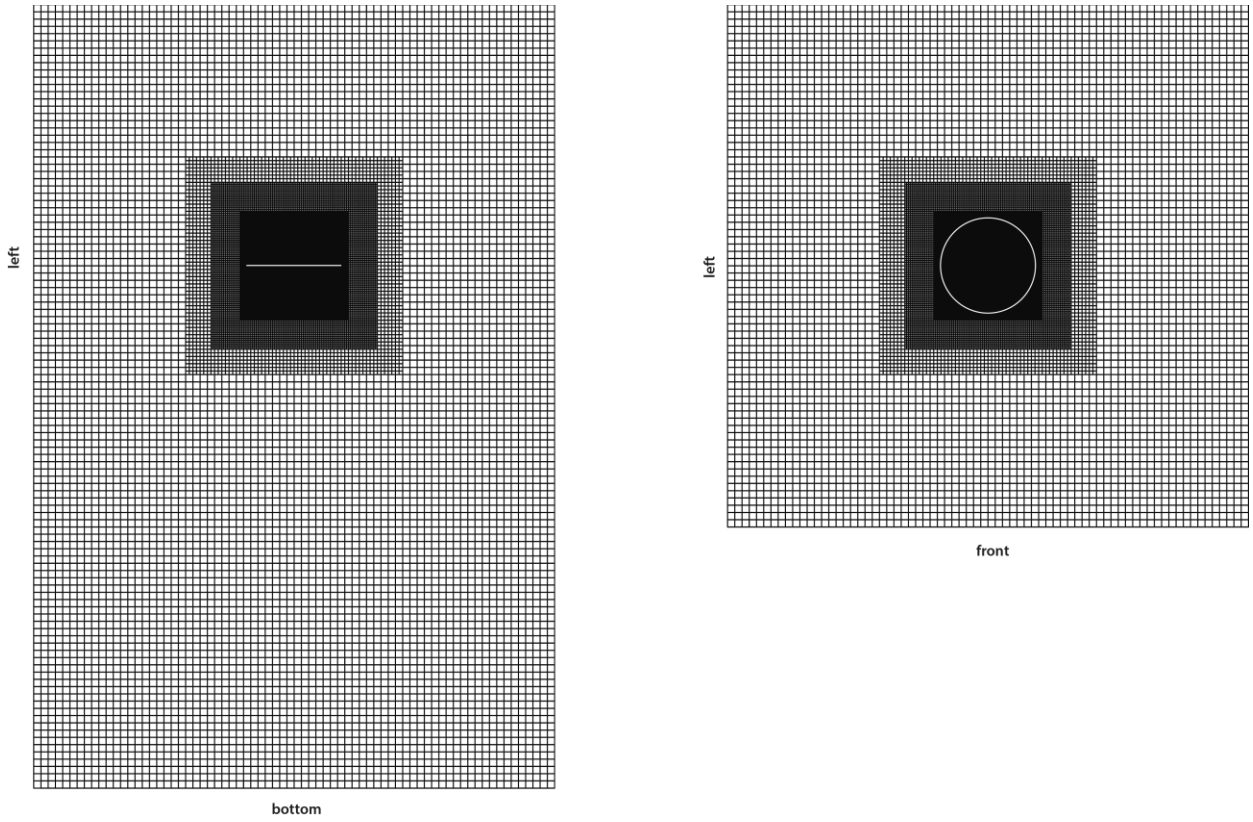

Figure 12. RotCFD unstructured grid for isolated hover case (rotor disk indicated in white).

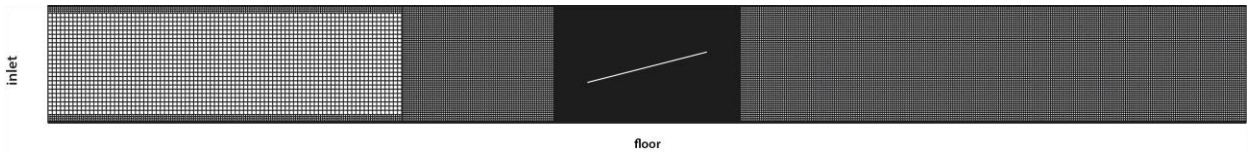

Figure 13. RotCFD unstructured grid for MARSWIT forward flight cases (rotor disk indicated in white).

The highest grid density (surrounding the rotor) is equal to the grid density for the isolated hover cases. The small computational domain allowed for relatively higher average grid density throughout the domain. The grid density near the walls is increased to accommodate the boundary layer. RotCFD is not expected to be able to properly model the boundary layer because of insufficient grid refinement at the walls, but nevertheless, the inevitable "observed boundary layer" can adversely affect the flow field in the tunnel if not properly accounted for.

Results

Figure 14 shows the velocity contour lines (m/s) of a representative isolated hover case. Only 1-atmosphere hover tests are correlated with experimental values, and observed tunnel test differences at various pressures are discussed in depth in Ament and Koning [2].

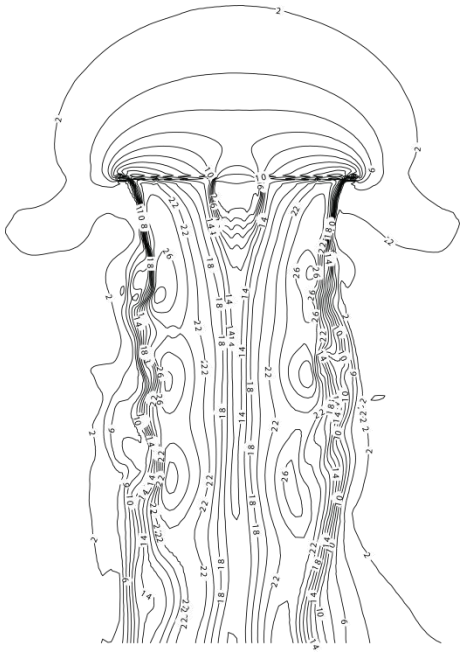

Figure 14. Isolated hover velocity contour lines (m/s).

Isolated Hover Results at 1 Atmosphere: Comparison With Experiment

McCoy and Wadcock [22] performed dual-rotor isolated hover testing for the AWT rotor. Testing at NASA Ames was also performed using a single-rotor setup. Both tests only recorded thrust values (no power or torque values). Figure 15 shows the single-rotor and dual-rotor (co-rotating) isolated hover thrust values versus RPM. Figure 16 shows the single-rotor and dual-rotor (co-rotating) isolated hover power values versus RPM.

The correlation with thrust for both single- and dual-rotor experiments is satisfactory.

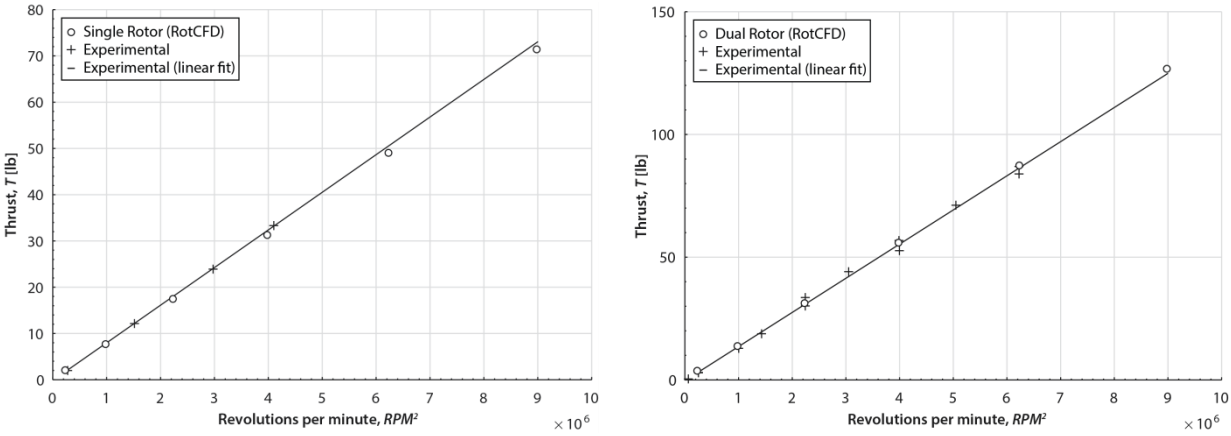

Figure 15. Isolated hover thrust comparison (left: single; right: dual) with experimental values.

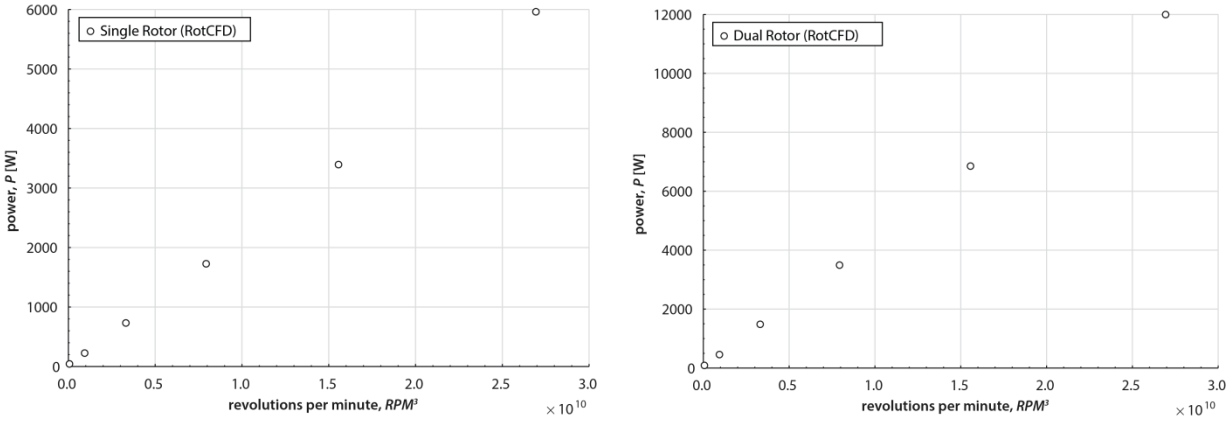

Figure 16. Isolated hover power (left: single; right: dual).

Reduced Pressure Isolated Hover Results

Figure 17 and Figure 18 include the performance results at 7 mbar for thrust and power. The dramatic reduction in thrust is observed as expected. At the time of writing, reduced-pressure isolated rotor test results were not available. These can provide critical insights into Reynolds number effects and testing difficulties at very low densities and pressures.

Figure 18 shows the same data points expressed as thrust versus power for both 1018-mbar and 7-mbar simulations. Besides the dramatic reduction in attainable thrust, the increase in power at low pressure is evident. A polynomial fit through the 1018-mbar data is drawn to allow comparison between the difference in slope for the rotor performance at 7 mbar and 1018 mbar. The only 1018-mbar data point visible in Figure 18 is at 500 RPM, the lowest simulated RPM.

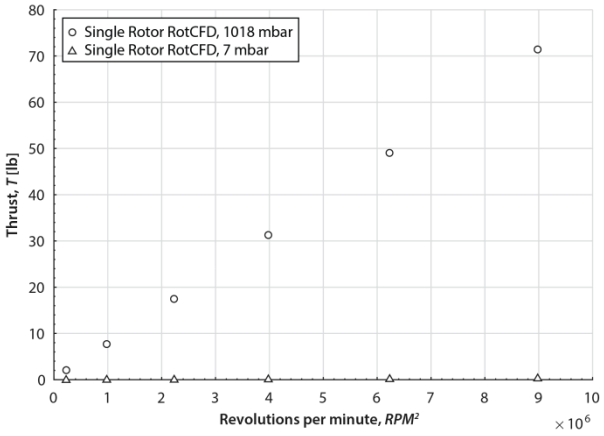

Figure 17. Isolated hover thrust comparison (single rotor).

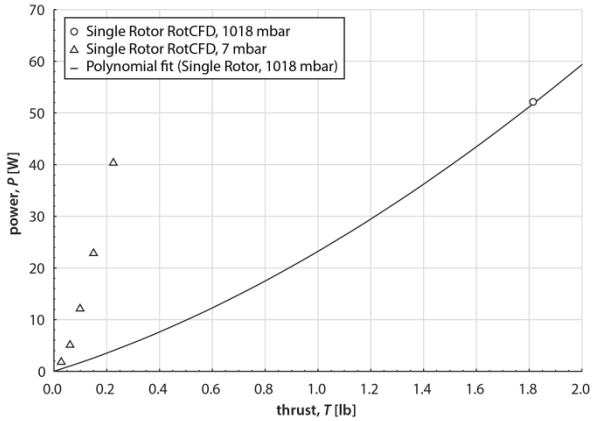

Figure 18. Thrust versus power comparison (single rotor).

Conclusions and Recommendations

The rotor model presented is extensively used to generate comparisons in the paper by Ament and Koning [2], following the experimental testing with the AWT rotor at various pressures in the PAL by Ament et al. [4]. The in-depth discussion of the comparison of the results in the Martian Surface Wind Tunnel (MARSWIT) in the PAL are also presented in this paper. This is primarily because the rotor results are hard to discuss without the experimental values and vice versa. The very low Reynolds number range is not yet well understood and presents various challenges; the rotor model is used to provide confidence in experimental MARSWIT forward flight results, particularly when testing at reduced pressure.

The correlation with thrust for both single- and dual-rotor isolated hover experiments at 1 atmosphere is satisfactory. The power values could not be compared to experimental values as they are not available at the time of writing.

The reduced pressure simulations show a reduction in lift (mostly due to the reduction in pressure) and an increase in power (when compared to equal thrust at 1 atmosphere). A reduction in lift due to Reynolds number effects is observed, but not to the same extent as the drag increase. The drag increase, and therefore the increase in torque and power observed, is due to Reynolds number effects, which are strongly represented in the 2D airfoil polars. The absence of transition at very low pressures, here 7 mbar, results in laminar separation without reattachment, as described by Koning et al. [23] for the MH airfoil deck generation.

References

[1] Balaram, J. and Tokumaru, P. T., "Rotorcrafts for Mars Exploration," *11th International Planetary Probe Workshop*, 2014.

[2] Ament, G. A. and Koning, W. J. F., "Isolated Rotor Forward Flight Testing From One Atmosphere Down to Martian Atmospheric Densities," *AHS Conference on Aeromechanics Design for Transformative Vertical Flight*, 2018.

[3] Koning, W. J. F., Johnson, W., and Allan, B. G., "Generation of Mars Helicopter Rotor Model for Comprehensive Analyses," *AHS Aeromechanics Design for Transformative Vertical Flight*, 2018.

[4] Ament, G. A., Koning, W. J. F., and Meyn, L., "Isolated Rotor Forward Flight Testing From One Atmosphere Down to Martian Atmospheric Densities," NASA CR-2018-219736, 2018.

[5] Young, L. A., and Aiken, E. W., "Vertical Lift Planetary Aerial Vehicles: Three Planetary Bodies and Four Conceptual Design Cases," *27th European Rotorcraft Forum*, 2001.

[6] Young, L. A., Aiken, E. W., Derby, M., Demblewski, R., and Navarrete, J., "Experimental Investigation and Demonstration of Rotary-Wing Technologies for Flight in the Atmosphere of Mars," *58th Annual Forum of the AHS International*, 2002.

[7] Corfeld, K. J., Strawn, R. C., and Long, L. N., "Computational Analysis of a Prototype Martian Rotorcraft Experiment," *AIAA Applied Aerodynamics Conference*, 2002.

[8] Drela, M., "XFOIL: An Analysis and Design System for Low Reynolds Number Airfoils," *Low-Reynolds Number Aerodynamics*, 1989.

[9] Leishman, G. J., *Principles of Helicopter Aerodynamics*, 2nd ed. New York: Cambridge University Press, 2006.

[10] Hoerner, S. F., *Fluid-Dynamic Drag: Practical Information on Aerodynamic Drag and Hydrodynamic Resistance*. Hoerner Fluid Dynamics, 1965.

[11] Owen, P. R., and Klanfer, L., "On the Laminar Boundary Layer Separation From the Leading Edge of a Thin Aerofoil," Aeronautical Research Council London, 1953.

[12] Carmichael, B. H., "Low Reynolds Number Airfoil Survey, Volume 1," Capistrano Beach, California, 1981.

[13] Mueller, T. J., and DeLaurier, J. D., "Aerodynamics of Small Vehicles," *Annual Review of Fluid Mechanics*, vol. 35, no. 1, pp. 89–111, Jan. 2003.

[14] Mueller, T. J., *Fixed and Flapping Wing Aerodynamics for Micro Air Vehicle Applications*. American Institute of Aeronautics & Astronautics, 2001.

[15] Hoerner, S. F., and Borst, H. V., *Fluid-Dynamic Lift: Practical Information on Aerodynamic and Hydrodynamic Lift*. Hoerner Fluid Dynamics, 1985.

[16] Schmitz, F. W., "Aerodynamics of the Model Airplane. Part 1 - Airfoil Measurements," Huntsville, AL, 1967.

[17] Rumsey, C. L., and Spalart, P. R., "Turbulence Model Behavior in Low Reynolds Number Regions of Aerodynamic Flowfields," *38th AIAA Fluid Dynamics Conference and Exhibit*, 2009, p. 5.

[18] Rajagopalan, R. G. et al., "RotCFD - A Tool for Aerodynamic Interference of Rotors: Validation and Capabilities," *American Helicopter Society International - Future Vertical Lift Aircraft Design Conference 2012*, pp. 311–327.

[19] Koning, W. J. F., Acree, C. W., and Rajagopalan, G., "Using RotCFD to Predict Isolated XV-15 Rotor Performance," *American Helicopter Society International - AHS Specialists' Conference on Aeromechanics Design for Vertical Lift*, 2016.

[20] Young, L. A., Yamauchi, G. K., and Rajagopalan, G., "Simulated Rotor Wake Interactions Resulting From Civil Tiltrotor Aircraft Operations Near Vertiport Terminals," *51st AIAA Aerospace Sciences Meeting including the New Horizons Forum and Aerospace Exposition*, 2013.

[21] Rajagopalan, R. G., Thistle, J. R., and Polzin, W. J., "The Potential of GPU Computing for Design in RotCFD," *AHS Technical Meeting on Aeromechanics Design for Transformative Vertical Flight*, 2018.

[22] McCoy, M. and Wadcock, A. J., "Documentation of the Recirculation in a Closed-Chamber Rotor Hover Test," NASA TM–2016-219162, 2016.

[23] Koning, W. J. F., Johnson, W., and Allen, B. G., "Generation of Mars Helicopter Rotor Model for Comprehensive Analyses," *AHS Aeromechanics Design for Transformative Vertical Flight*, 2018.